Graphene quantum dots, graphene non-circular n–p–n-junctions: Quasi-relativistic pseudopotential approach

H. V. Grushevskaya* and G. G. Krylov†
Physics Department, Belarusian State University, 4 Nezalezhnasti Ave., 220030 Minsk, BELARUS
S. P. Kruchinin
Bogolyubov Institute for Theoretical Physics, Metrologichna str. 14-b, 03143 Kiev,UKRAINE
B. Vlahovic
North Carolina Central University, Durham, NC, USA
J. K. Freericks
3Department of Physics, Georgetown University, Washington, DC 20057, USA

We have constructed a continuous model of graphene quantum dot (GQD) as the hydrodynamic limit of the discrete model of n–p–n graphene junction in the form of a rhombic supercell on the graphene plane. The topological type of the proposed GQD-model corresponds bijectively to the GQD-edge topology and can be similar to a sphere or torus. The Hamiltonian of the discrete model of n–p–n graphene junction is chosen to be the Dirac–Weyl type with one Dirac point and 6 pairs of Weyl nodes–antinodes in the folding-zone approximation. The bending-band structure of the proposed GQD-model is ensured by a GQD pseudopotential barrier, which is given by a set of well pseudopotentials for individual carbon atoms of the GQD. The main specific feature of the structure of electron levels of both spherical and toroidal GQDs is the self-similar energy bands located subsequently one behind another on the energy scale. The atom-like distribution of the electron density is realized from the geometric viewpoint only for toroidal GQDs due to the absence of the curvature for a torus. Though the quasi-zero-energy band exists for spherical and toroidal GQDs, no electron density is present on this band for toroidal GQDs. This causes the formation of a pseudogap between the hole and electron bands, because of the absence of the electron density at the quantum dot center like the case of an ordinary atom. However, the confinement of the electron density is observed for both spherical and toroidal GQDs.

I. INTRODUCTION

Chemically synthesized nanoscale graphene quantum dots (GQDs) have the form of a quasicircle with a radius in the interval from 3 nm to 10 nm [1]. The Schrödinger Hamiltonian with a confined parabolic potential well was used to calculate the energy levels within a continuous model of quantum dot (QD) [2]. But, the results of such simulations describe correctly only the low-lying part of the dot energy spectrum.

In [3], circular n–p–n and p–n–p junctions with radii up to 8 nm in a graphene monolayer have been formed on electrostatically charged surface defects. In [4] similar junctions but with a radius of about $r_{\rm dot} \sim 150$ nm utilizing scanning tunneling microscopy (STM) have been formed. These junctions are called electrostatically confined GQDs without a physical termination. The atomic-like distribution of the electron (hole) density in such GQDs is fitted by a continuous Thomas–Fermi-like approximation for a potential $U(r)$ confining electrons (holes): $U(r) = \mathrm{sgn}(n)\hbar v_F\sqrt{\pi|n(r)|}$. Here, $n(r)$ is the hole density for n–p–n junctions or the electron density for p–n–p junctions, and v_F is the Fermi velocity. Electrically confining potentials are chosen in the Gaussian shape for the radius of the cantilever STM tip $r_{tip} \leq 20$ nm or in cos-shape for $r_{tip} \geq 100$ nm [6],[7].

The experimental results on the scattering of electrons (holes) in circular n–p–n and p–n–p junctions were well described only at a GQD-center within a continuous pseudo-Dirac GQD-model (pseudo-Dirac massless fermion Hamiltonian) with parabolic potential $\mathrm{sgn}(n(r))\kappa r^2$ [4, 5]. In such an approach the equivalence has been assumed on the change of the problem of motion of holes and electrons in the potential well ($\mp\kappa r^2$) to the problem on scattering by the barrier ($\pm\kappa r^2$) (upper and lower signs for holes and electrons respectively) with a sufficiently high repulsive potential at the distance L far from the boundary of the quantum point so that $L \gg r_{\rm dot}$. Naive considerations of the equivalence of such a change lead to the following unpleasant feature of the model as the appearance of false hole states (spurious states) at $r = 0,\ L$ (see section "Methods" in [4]) stipulated by the effective infiniteness of the well that is not a good choice for any Dirac problem. The usage of the massless pseudo Dirac equation with a finite-height step-like radial positive potential (barrier for electrons and well for holes) allows one to perform simulations for the electron density in the circular graphene n–p–n junctions of sizes of 5.93 nm and 2.76 nm [3]. Despite the roughness of such continuous model in comparison with the parabolic barrier model, the theory and experiment should, at least, qualitatively coincide, if the assumption about the formation of a circular n–p–n junction, by adding a step barrier to the Dirac cone, is valid. But the pseudorelativistic simulation results satisfactory describe only the high-energy GQD-levels, and the discrepancy between estimated and observed data grows with the GQD radius. To understand the nature of GQDs, some simplified continuous Dirac GQD models are in use. At the present time, except for the intuitive considerations, there exists no logical substantiation of the continuous GQD models.

*Electronic address: grushevskaja@bsu.by
†Electronic address: krylov@bsu.by

A feature of realistic GQDs with a zigzag termination is a band of quasi zero-energy levels [8]. However, the continuous Dirac GQD-model, which takes into account the differences between zigzag and armchair edge topologies by the so called zigzag boundary condition (ZZBC), predicts a pure zero-energy level only [9]. The continuous GQD model with an infinite mass boundary condition (IMBC) is insensitive to the edge topology and does not predict the quasi zero energy band.

For an electrostatically confined GQD, we can select a tip-induced potential amplitude so that a diameter of the Landau level state for graphene be more than the band bending region. By this, we get a magnetic confinement to be comparable with the geometric one for some value B_c of the magnetic field. In this case, the orbital levels converge under the action of the magnetic field and become Landau levels [10]. So, we should expect the appearance of effects of a topology of the GQD-edge in the form of the quasi-zero-band in the structure of GQD-levels. Indeed, the experiments demonstrate the appearance of quadruplet levels in the band structure of an electrostatically confined quantum dot in the graphene monolayer as the charging peaks of the difference conductivity at the GQD center and outside it under the action of a magnetic field B_c [5]. However, the non-relativistic tight binding (TB) calculations connect those peaks with radial orbital levels, rather than with the quasi-zero-band. TB calculations predict the orbital splitting $E_o \sim 10$ meV and the splitting energy $E_v \sim 3$ meV for a valley of orbitals. The experimentally measured distance $E_q \sim 20$ meV between the quadruplets of energy levels differs practically twice from the orbital splitting E_o, and the difference cannot be compensated by the small orbitals valley splitting energy E_v and by the Zeeman splitting, which is significantly less than E_v. In addition, TB calculations cannot predict the 4-fold degeneration of the GQD-levels. No mechanism, whose consideration in the TB calculation would increase the distance between the quasi-zero-energy levels from 10^{-5} up to ~ 5 meV and would group that in four, is known.

A GQD model with IBMC can be modernized by the introduction of the Keldysh-type effects with zero dimension of a GQD [11]. They remove the excitonic pairing instability holding for graphene [12]. But, for a quasi-zero-energy band emerging in the continuous GQD model with IMBC, the binding energy of an exciton is at least 4 times less (about 50 meV), than the minimum voltage (electrostatic potential) 200-400 meV, at which the generation of a charging quadruplet starts. The main drawback of the model with IMBC is the possibility of the excitation of a continuous excitonic spectrum in the absence of magnetic fields under the action of electric fields created at the voltage of at least 100 meV.

So, the results of the pseudo-Dirac massless fermion theory (as well as TB calculations) and experimental data can be directly compared near a GQD center. There are no satisfactory continuous models to study GQDs of large sizes. Moreover, the principal problem of the known theories of GQDs with a zero-energy band (continuous models) or with quasi-zero-energy band (TB) is that the theoretically complete confinement is absent due to the Klein tunneling, despite the fact that the step- or parabolic potential confine the electron density inside a quantum dot.

The electrostatic geometric confinement in a graphene monolayer allows one to finely tune the charge localization and scattering in graphene-based devices. However, because of the absence of proper models, in which a quasi-zero-energy band emerges, by leading to the charging peaks of differential conductance, a realization of devices based on the tailored charge confinement in a graphene monolayer is remained challenging.

To solve the problems, we need to construct a correct model of electrostatically confined GQD in the continuous limit of a discrete quasirelativistic GQD model based on the tight binding approximation of quasirelativistic massless fermion graphene models.

In this paper, we present a discrete model of GQD including the Dirac point K(K') and six Weyl nodes–antinodes pairs and find its continuous limit to describe realistic electrostatically confined GQDs. We look for a GQD pseudopotential barrier, which is given by a set of well potentials for distinct carbon atoms of the GQD, and propose two topologically different scenarios of the confinement in GQD-models.

II. MODEL OF ELECTRICALLY-CONFINED GRAPHENE QUANTUM DOT AND THEORY

A graphene monolayer quantum dot consisting of carbon atoms is shown schematically in fig. 1a. Let a model GQD be considered as a "large atom" . Its core i-th electrons, by definition, are p_z-electrons of j-th C atoms, $j \neq i$. The k-th p_z-electron of k-th C atom plays the role of an external valent electron of GQD. Let the k-th C atom be placed at the lattice site with a radius-vector $\vec{L}_k$. The radius vector $\vec{r}$ will be calculated on respect to nearest lattice site and is a radius vector of the electron in the atom. The radius vector $\vec{X}_k$ of the valent electron of k-th atom is given by the expression

$$\vec{X}_k = \vec{L}_k + \vec{r}. \tag{II.1}$$

A model graphene quantum dot has been constructed in the following way. The graphene primitive cell has basic vectors $\vec{b}_1 = a(3/2, \sqrt{3}/2)$, $\vec{b}_2 = a(3/2, -\sqrt{3}/2)$ and two atoms (A and B) in the cell. Here a is the length of sp^2-hybridized C–C bond. We construct a supercell consisting of $(2n_1+1)*(2n_2+1)$ primitive cells for $n_1 = 25, n_2 = 25$, that is shown in fig. 1b.

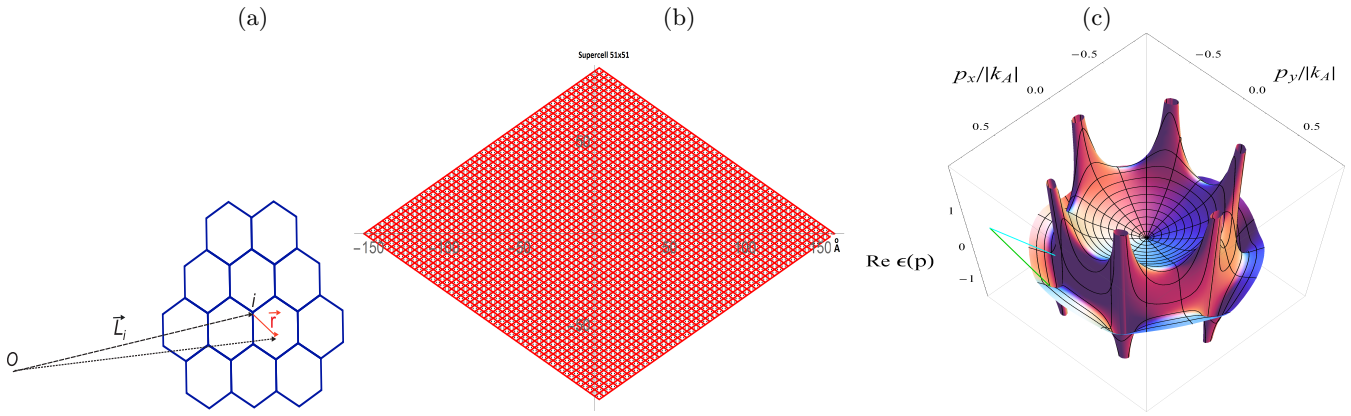

FIG. 1: Scheme of a graphene quantum dot: the i-th atom C of a GQD is located at the i-th site with radius vector $\vec{L}_i$, and $\vec{r}$ is a radius vector of the p_z-electron relative to the i-th lattice site, O is a reference point (a). Graphene quantum dot supercell includes 51×51 primitive cells (100×150 Å) (b). Splitting of Dirac cone replicas for graphene in the Dirac–Hartree–Fock quasirelativistic approximation, q^4 approximation for the exchange interactions. One of the six pairs of Weyl nodes–antinodes: source and sink are indicated (c).

A. "Folding zone" approximation

The quantization conditions can be obtained by "folding zones" (like for single walled carbon nanotubes (CNT)) applied in both directions allowing by a quantum-dot symmetry. The quantization condition for the collective excitation with a wave-vector $\vec{k} = (k_x, k_y)$ for CNT with a chiral vector $\vec{C}$ reads

$$\vec{k} \cdot \vec{C} = 2\pi m, \quad m = 0, 1, \ldots, N, \tag{II.2}$$

where N is the number of graphene hexagonal unit cells within a CNT unit cell [13]. The condition (II.2) is the so called "Born–von–Karman" condition which makes a CNT Brillouin zone to be quantized.

Opposite to the case of cylindrical topology of nanotubes, QDs can be constructed with two topologies (quantization conditions): sphere S^2 and torus $S^1 \times S^1$. These two topologies differ by the ratio of zigzag- and armchair-edges.

Quantization conditions for S^2 type GQD read

$$\begin{aligned} ((2n_1+1)\vec{b}_1 + (2n_2+1)\vec{b}_2) \cdot \vec{k} = 2\pi m_1, \ m_1 = -N_{dot}/2, \ldots, N_{dot}/2; \\ ((2n_1+1)\vec{b}_1 - (2n_2+1)\vec{b}_2) \cdot \vec{k} = 2\pi m_2, \ m_2 = -N_{dot}/2, \ldots, N_{dot}/2. \end{aligned} \tag{II.3}$$

Here $N_{dot} = (2n_1+1)(2n_2+1)$ is the total number of graphene hexagonal unit cells within the supercell. For the model GQD shown in fig. 1 the number of levels $(N_{dot}+1)^2$ is approximately equal to 6.7×10^6.

For the toroidal-type GQD we have to choose the following vectors as the basis vectors $\vec{C}_1 = (2n_1+1)\vec{b}_1$, $\vec{C}_2 = (2n_2+1)\vec{b}_2$ of the supercell. This results in the following systems for quantized wavevectors:

$$\begin{aligned} (2n_1+1)\vec{b}_1 \cdot \vec{k} = 2\pi m_1, \quad m_1 = -N_{dot}/2, \ldots, N_{dot}/2; \\ (2n_2+1)\vec{b}_2 \cdot \vec{k} = 2\pi m_2, \ m_2 = -N_{dot}/2, \ldots, N_{dot}/2. \end{aligned} \tag{II.4}$$

When using folding-zone approach to calculate GQD energies, one has to work with the whole rather than the first Brillouin zone. A wavevector $\vec{k}$ satisfying either (II.3) or (II.4) quantization conditions for different GQD types is indexed by two integers m_1, m_2. We associate such a vector $\vec{k}_{m_1,m_2}$ with the reduced wave vector $\vec{q}_{m_1,m_2}$ as the difference between $\vec{k}_{m_1,m_2}$ and the nearest Dirac point.

We use a model $\vec{k} \cdot \vec{p}$-Hamiltonian $\hat{H}_D$, for which the band structure of graphene is characterized by a single Dirac point and six Weyl pairs of nodes-antinodes [14],[15], in order to determine the energy levels $\epsilon(q_{m_1,m_2})$ of GQD in the folding-zone approximation. This graphene model is a quasirelativistic model in the q^4 approximation for the exchange interactions. Here $q = \left|\vec{p} - \vec{K}_{A(B)}\right|$, $K_A(K_B)$ designates a Dirac point K(K') of Brillouin zone. Crossing valent and conduction bands of the graphene model are represented in fig. 1c.

For every wave vector, being a solution of the conditions of quantization and belonging to the graphene Brillouin zone, there is the corresponding discrete energy level $\epsilon(q_{m_1,m_2})$ of GQD and the corresponding spinor wave function in the form of a plane wave $\psi(q_{m_1,m_2}) \propto \exp\left(\imath \vec{q}_{m_1,m_2} \cdot (\vec{r} + \vec{L}_k)\right)$.

We sort the energy levels $\epsilon(q_{m_1,m_2})$, in the energy increase order, by introducing an index i for the energies and wave vectors and introduce a formal index L_k according to the above presented wave function form. Therefore in what follows, we will denote the energies by $\epsilon_{L_k}(q_i)$. We emphasize that the energy does not depend upon L_k.

Thus, the following set of eigenenergies $\pm\epsilon_{L_k}(q_i)$ and eigenstates $\psi_i^{(0)}\left(\mp q_i, \vec{r}+\vec{L}_k\right) = e^{\mp\imath\vec{q}_i\cdot(\vec{r}+\vec{L}_k)}u(\vec{r}+\vec{L}_k)$ for quasi-particle excitations of GQD holds:

$$\left\{\pm\epsilon_{L_k}(q_i),\ \psi_i^{(0)}\left(\mp\vec{q}_i, \vec{r}+\vec{L}_k\right)\right\}_{i,k=1,\ldots,N_{dot}}, \tag{II.5}$$

where upper sign "+" is related to electrons and lower to "−" corresponds to holes.

In the following section we construct the pseudopotential for atoms C in GQD.

B. Continuous GQD model with pseudo-potential

Opposite to monolayer graphene where all electrons are paired, in GQD there are valent non-paired electrons. Therefore, to q^4 graphene approximation hamiltonian $\hat{H}_D$ [14],[15] one has to add pseudopotential operator $\sum_{j=1}^{n}\hat{\epsilon}^\dagger P_j$ [16, 17], where $\hat{\epsilon}^\dagger$ is a hole energy operator, P_j is a projection operator, n is a number of electrons in a system. Then we get an eigenproblem for the following Hamiltonian:

$$\hat{H}_D(\vec{r}_i)\psi_m(x_i) = \left(\epsilon_m - \sum_{j=1}^{n}\hat{\epsilon}^\dagger P_j\right)\psi_m(x_i), \tag{II.6}$$

where ϵ_m is a m-th eigenvalue of $\hat{H}_D(\vec{r}_i)$, $x_i = \{\vec{r}_i, \sigma_i\}$, σ_i is the spin of i-th electron. We use a representation where the operator $\hat{\epsilon}^\dagger$ is a matrix, which elements $\{\epsilon_{kc_i}\} \equiv \{\epsilon_{L_k - L_i}(q_{c_i})\}$ belong to the set (II.5). Here, on definition of a valent electron, $\epsilon_{kc_i} = 0$ at $k = c_i$. In this representation the equation (II.6) is an equation of motion for the valent k-th electron with a radius-vector $\vec{r}_k = \vec{r} + \vec{L}_k$:

$$\hat{H}_D\psi_k(\vec{r}+\vec{L}_k) + \sum_{i,c_i\neq k}^{N_{dot}-1}\epsilon_{kc_i}P_{c_i}\psi_{c_i}(\vec{r}+\vec{L}_k) = E_k\psi_k(\vec{r}+\vec{L}_k), \quad k = 1,\ldots,N_{dot}. \tag{II.7}$$

Since a GQD consists of sufficiently many atoms, one can construct a continuous GQD model as a hydrodynamic limit $\left|\vec{L}_{k+1} - \vec{L}_k\right| = a \to 0$, $r \to 0$ of our discrete GQD model. A radius-vector $\vec{R}$ of point in the continuous GQD model is defined by the following expression:

$$\vec{R} \in \left\{\vec{L}_k\right\}\Big|_{k=1}^{N_{dot}}. \tag{II.8}$$

A derivative $\frac{\partial}{\partial\vec{R}}$ for the continuous GQD model is determined in a following way:

$$\frac{\partial}{\partial\vec{R}}\Psi(\vec{R}) \stackrel{def}{=\!=} \left\{\frac{\psi_k(\vec{L}_{k+1}) - \psi_k(\vec{L}_k)}{\vec{L}_{k+1} - \vec{L}_k}\right\}\Big|_{k=1}^{N} = \left\{\frac{\psi_k(\vec{L}_k + \vec{a}) - \psi_k(\vec{L}_k)}{\vec{a}}\right\}\Big|_{k=1,\ a\to 0}^{N_{dot}}, \tag{II.9}$$

where $\Psi(\vec{R})$ is a GQD wave function defined by the following expression:

$$\Psi\left(\vec{R}\right) \in \left\{\psi_k(\vec{r}+\vec{L}_k)\right\}\Big|_{k=1,r=a}^{N_{dot}}. \tag{II.10}$$

Using the definition (II.9) one can determine a convolution $\vec{\sigma}\cdot\frac{\partial}{\partial\vec{R}}\Psi_v^{dot}$ of the derivative with 2D-vector of Pauli matrixes $\vec{\sigma} = (\sigma_x, \sigma_y)$ for a v-th electron as

$$\vec{\sigma}\cdot\frac{\partial}{\partial\vec{R}}\Psi_v(\vec{R}) = \sum_{i=1}^{2}\sigma_i\frac{\partial}{\partial x_i}\Psi_v = \sum_{i=1}^{2}\sigma_i\left\{\frac{\psi_v(\vec{L}_k + (\vec{e}_i,\vec{a})\vec{e}_i) - \psi_v(\vec{L}_k)}{(\vec{e}_i,\vec{a})}\right\}\Big|_{k=1,\ a\to 0}^{N_{dot}} \equiv \vec{\sigma}\cdot\vec{\nabla}_{\vec{R}}\Psi_v(\vec{R}), \tag{II.11}$$

where $\vec{e}_i,\ i = x,\ y$ are orthonormal vectors along the coordinate axes $X,\ Y$; $(\cdot,\cdot)$ is a scalar product, $\vec{x}_i = x_i\vec{e}_i$. Then, in the hydrodynamic limit the system of equations (II.7) taking into account the equality $E_k\psi_k(\vec{r}+\vec{L}_k) = i\hbar\frac{\partial}{\partial t}\psi_k(\vec{r}+\vec{L}_k)$, can be rewritten as

$$\left\{\hat{H}_D\psi_k(\vec{r}+\vec{L}_k) + \sum_{c\neq k}\epsilon_{kc}\psi_c(\vec{r}+\vec{L}_k) = E\psi_k(\vec{r}+\vec{L}_k)\right\}_{k=1,r\to a}^{N_{dot}}. \tag{II.12}$$

Using the definitions (II.8 – II.10) and a definition of the projection operator in notations of Dirac ket-, bra-vectors $\left\langle \vec{R}\right| \Psi_j\rangle \equiv \Psi_j(\vec{R})$ one gets an equation of motion for the valent v-th electron of the continuous GQD model with a pseudopotential V_{GQD}:

$$\left\langle \vec{R}\right| \hat{H}_D \left|\Psi_v\right\rangle + \sum_{i=1,c_i\neq v}^{N_{dot}-1} \left\langle \vec{R}\right| \Psi_{c_i}\rangle \, \epsilon_{c_i}(\vec{R}) \left\langle \Psi_{c_i}\right| \Psi_v\rangle = E \left\langle \vec{R}\right| \Psi_v\rangle \,. \tag{II.13}$$

Here $V_{GQD} \equiv \sum_{i=1,c_i\neq v}^{N_{dot}-1} |\Psi_{c_i}\rangle \, \epsilon_{c_i}(\vec{R}) \, \langle\Psi_{c_i}|$, a matrix $\epsilon_{c_i}(\vec{R})$ is determined by the expression $\epsilon_{c_i}(\vec{R}) \in \{\pm\epsilon_{L_k-L_i}(q_{c_i})\}_{k=1,\ldots,N_{dot}}$ entering the expression (II.5). A scalar product $\langle\Psi_{c_i}|\,\Psi_v\rangle = \int \langle\Psi_{c_i}|\,\vec{R}'\rangle \left\langle \vec{R}'\right|\Psi_v\rangle \; d\vec{R}'$ of the wave-functions $|\Psi_{c_i}\rangle$ and $|\Psi_v\rangle$ of core and valent electrons of GQD and, consequently the operator V_{GQD} are constructed on a basic set of functions entering the expression (II.5):

$$\langle\Psi_{c_i}|\,\Psi_v\rangle = \sum_{k=1}^{N_{dot}} {\psi^{(0)}}^{\dagger}_{L_k}\left(\mp\vec{q}_{c_i},\vec{L}_k\right) \psi^{(0)}_{L_k}\left(\mp\vec{q}_v,\vec{L}_k\right) \tag{II.14}$$

and

$$\begin{aligned} \langle\Psi_{c_n}|\,V_{GQD}(\vec{R})\,|\Psi_{c_m}\rangle &= \sum_{i=1,c_i\neq v}^{N_{dot}-1} \langle\Psi_{c_n}\,|\Psi_{c_i}\rangle\,\epsilon_{c_i}(\vec{R})\,\langle\Psi_{c_i}|\,\Psi_{c_m}\rangle \\ = \sum_{i=1,c_i\neq v}^{N_{dot}-1} \sum_{k,l=1}^{N_{dot}} {\psi^{(0)}}^{\dagger}_{L_k}\left(\mp\vec{q}_{c_n},\vec{L}_k\right) \psi^{(0)}_{L_k}\left(\mp\vec{q}_{c_i},\vec{L}_k\right) \epsilon_{L_k-L_l}(q_{c_i}) {\psi^{(0)}}^{\dagger}_{L_l}\left(\mp\vec{q}_{c_i},\vec{L}_l\right) \psi^{(0)}_{L_l}\left(\mp\vec{q}_{c_m},\vec{L}_l\right). \end{aligned} \tag{II.15}$$

To solve the eigenproblem when taking into account the expressions (II.14, II.15), one needs a matrix form of eq. (II.13):

$$\sum_j \langle\Psi_{c_n}|\,\hat{H}_D(\vec{R})\,\left|\Psi_{c_j}\right\rangle\left\langle\Psi_{c_j}\right|\,\Psi_v\rangle + \sum_m \langle\Psi_{c_n}|\,V_{GQD}(\vec{R})\,|\Psi_{c_m}\rangle\,\langle\Psi_{c_m}|\,\Psi_v\rangle = E\,\langle\Psi_{c_n}|\,\Psi_v\rangle\,. \tag{II.16}$$

Since in the Dirac point $K(K')$ $q\to 0$, as a basic set of wave functions one can use the set $\{\psi_k = \exp(i\vec{q}\cdot(\vec{r}+\vec{L}_k))\}$. In this long-wave case the pseudopotential (II.15) can be approximately estimated as

$$V_{i,L_k}(\vec{r}) \approx -2\pi \int_0^q e^{i\vec{q}\,'\cdot(\vec{r}+\vec{L}_k)} \epsilon_{L_k}(q')\delta(q_i-q')dq', \quad q\to 0,\ i\neq k, r\leq a. \tag{II.17}$$

As a size of the carbon atom we can choose the one half of the length of C–C bond $l_{\rm C}$: $a = 0.5\; l_{\rm C}$ ($a\sim 0.71$ Å). We use the following formula for the derivative of the Heaviside Θ-function:

$$\frac{d\Theta(q-q_i)}{dq} = \delta(q-q_i) \tag{II.18}$$

where $\delta(q-q_i)$ is the Dirac δ-function. After substitution of (II.18) into the expression (II.17) the integration gives in the limit $q = 2\pi/R \to 0$ the scattering potential of the form

$$V_{i,L_k}(\vec{r}) = -2\pi\epsilon_{L_k}(q_i)\Theta\left(\lambda_i - R\right)\Theta(a-r),\ i\neq k, \vec{L}_k = \vec{R}-\vec{r}. \tag{II.19}$$

where $\lambda_i = \frac{2\pi}{q_i}$. The potential (II.19), some well-known model potentials and a potential reconstructed based on experimental data are shown in fig. 2. For a finite set of eigenenergies $\epsilon_{L_k}(q_i)$ the potential results in some staircase-like potential which resemble the experimental one shown in fig. 2b.

III. RESULTS AND DISCUSSION

A. Emergence of quasi zero-energy band

In order to evaluate the influence of a work function difference between the tip and the sample on the pattern of a distribution of the electron density in STM-experiments, we study a local density of states (LDOS) on two energy scales. For the torus and sphere topologies, we choose the low- and high-energy ranges $0.24\div 0.92$ eV and $0.68\div 2.94$ eV and, respectively, $0.24\div 1.22$ eV and $2.98\div 3.26$ eV. The scales were obtained in the following way. For the low-energy range, we got the solutions of the conditions of quantization (II.3), (II.4) for $m_1,\ m_2\in[-25,25]$, which corresponds to the choice of 40 lowest energy levels from 2601. For the high-energy interval, we determined the solutions of the

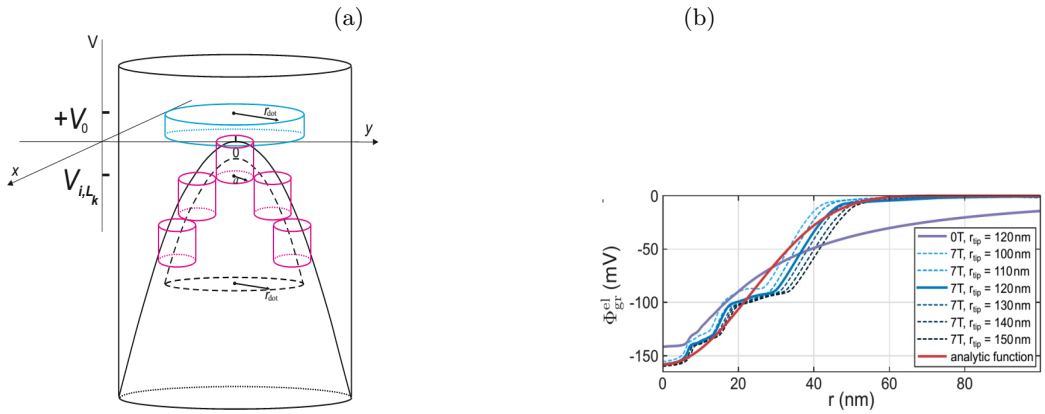

FIG. 2: (a) Model scattering potentials for the quantum dot (n–p–n junction) of radius $r_{\rm dot}$: a long-wave approximation of pseudopotential $V_{i,L_k} = -\epsilon_{L_k}(q_i)\Theta(\lambda_i - R)\,\Theta(a - r)$ (red curves), $L_k = |\vec{R} - \vec{r}|$; a parabolic potential $(-\kappa r^2)$ with a large repulsive potential outside the graphene quantum dot [4] (black curves); a cylindrical barrier potential $V = +V_0\Theta(r_{\rm dot} - R) \geq 0$, $V_0 > 0$ (blue curves) see e.g., [18] and references therein. (b) Reconstructed potential base on experimental data of [5].

conditions of quantization (II.3), (II.4) for $m_1,\ m_2 \in [-12, 12]$, which corresponds to the choice of 40 lowest energy levels from 625. Two bands of levels referred to small and large energy scales in the folding-zone approximation are presented in Tables I and II, respectively. The indices of eigenstates, wave numbers, and calculated eigenenergies in the folding-zone approximation are given in the first three or four columns of these tables. The resulting eigenenergies in the pseudopotential approximation (again in a sorted order) are shown in the last column of the tables. They do not correspond already to states with definite wave numbers $\vec{k}_i$.

Comparing the structures of the levels $E_D(\vec{k}_i)$ and $E^{(0)}(\vec{k}_i)$, $i = 1, \ldots, 40$ for a Dirac GQD-model and our GQD-model with Weyl nodes-antinodes, respectively, in the folding-zone approximation in Table I, we conclude that the Weyl nodes-antinodes decrease the degree of degeneration of the levels p_d. The effects of a topology and a symmetry related to it manifest themselves in different maximum values of the degree of degeneration p_d of the levels for the sphere and torus topologies in the folding-zone approximation. So, the maximum values $\max(p_d)$ are equal to 4 and 12 for the Dirac spherical and toroidal GQD-models, respectively. In the case of Weyl nodes-antinodes, $\max(p_d)$ takes values of 4 and 6 for the spherical and toroidal GQD-models, respectively. According to Tables I and II, the pseudopotential breaks the symmetry and completely removes the degeneration of levels $E^{(0)}(\vec{k}_i)$, $i = 1, \ldots, 40$ so that the resulting spectrum $E_i^{(1)}$, $i = 1, \ldots, 40$, consists of two bands. The lower energy band is formed of levels located near the zero energy $E = 0$ and is a quasi-zero-energy band, as can be seen in fig. 3, where the spectra for both toroidal and spherical GQDs in the pseudopotential approximation hold a very narrow quasi-zero-energy band.

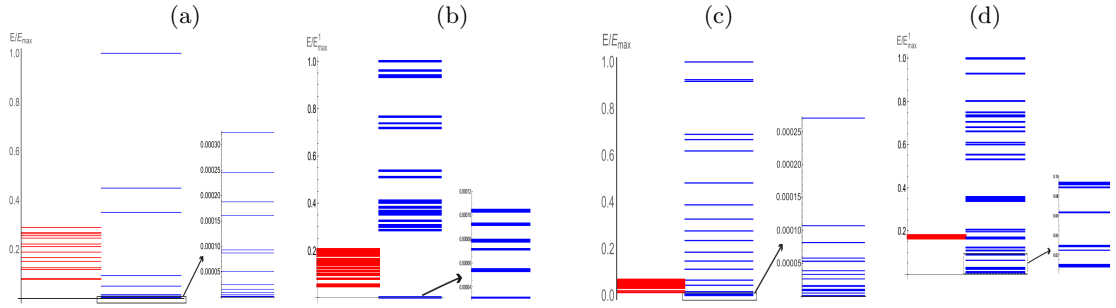

FIG. 3: Energy spectra for $S^1 \times S^1$ (a, b) and S^2 (c, d) GQDs on low- (a, c) and high-energy scales (b, d). Left spectra are in the folding-zone approximation, right spectra are in the pseudopotential approximation. Spectra are normalized to the largest value of the right spectrum.

B. Toroidal quantum dot

Electrons in a toroidal GQD can be in states of the following types: 1) states of the type of standing waves which are characteristic for atoms and are determined by the zero curvature of a torus, as one can see in figs. 4(upper row); 2) states strongly localized on discrete levels by the pseudopotential confinement (see figs. 4(middle row)); and 3) confined states weakly localized because of the destructive interference (see figs. 4(lower row)).

TABLE I: A set of eigenenergies $E^{(1)}$ for the continuous model GQD with the pseudopotential and its folding-zone approximation $E^{(0)}(\vec{k})$ with the torus (a) and sphere (b) topologies on sufficiently small energy scales. All energies are given in eV. The degenerate levels are shown by a bold font and italics. For comparison, we give the eigenenergies $E_D(\vec{k})$ for the Dirac GQD in the folding-zone approximation.

(a)

No.	$\vec{k}/\lvert K_A\rvert$	$E_D(\vec{k})$	$E^{(0)}(\vec{k})$	$E^{(1)}$
1	$(0., -0.017)$	**0.244**	0.238	1.05×10^{-9}
2	$(0., 0.017)$	**0.244**	0.250	1.26×10^{-9}
3	$(0.005, -0.026)$	*0.373*	*0.361*	4.80×10^{-8}
4	$(-0.005, -0.026)$	*0.373*	*0.361*	6.38×10^{-8}
5	$(-0.020, 0.017)$	*0.373*	*0.361*	8.23×10^{-8}
6	$(0.020, 0.017)$	*0.373*	*0.361*	1.31×10^{-7}
7	$(0.025, 0.008)$	*0.373*	*0.361*	4.77×10^{-7}
8	$(-0.025, 0.008)$	*0.373*	*0.361*	3.223×10^{-6}
9	$(0.005, 0.026)$	*0.373*	**0.384**	5.70×10^{-6}
10	$(-0.005, 0.026)$	*0.373*	**0.384**	6.53×10^{-6}
11	$(-0.020, -0.017)$	*0.373*	**0.384**	1.51×10^{-5}
12	$(0.02, -0.017)$	*0.373*	**0.384**	2.86×10^{-5}
13	$(0.025, -0.008)$	*0.373*	**0.384**	4.81×10^{-5}
14	$(-0.025, -0.008)$	*0.373*	**0.384**	7.556×10^{-5}
15	$(0., -0.034)$	**0.488**	0.465	1.57×10^{-4}
16	$(0., 0.034)$	**0.488**	0.512	2.68×10^{-4}
17	$(-0.040, 0.017)$	*0.614*	*0.581*	2.86×10^{-4}
18	$(0.040, 0.017)$	*0.614*	*0.581*	4.93×10^{-4}
19	$(-0.040, -0.017)$	*0.614*	**0.650**	5.77×10^{-4}
20	$(0.040, -0.017)$	*0.614*	**0.650**	7.55×10^{-4}
21	$(0., -0.052)$	**0.732**	*0.682*	9.96×10^{-4}
22	$(0.045, 0.026)$	**0.732**	*0.682*	1.16×10^{-3}
23	$(-0.045, 0.026)$	**0.732**	*0.682*	1.20×10^{-3}
24	$(-0.020, -0.052)$	*0.785*	**0.756**	1.57×10^{-3}
25	$(0.020, -0.052)$	*0.785*	**0.756**	1.90×10^{-3}
26	$(0., 0.052)$	**0.732**	*0.787*	1.15×10^{-2}
27	$(0.045, -0.026)$	**0.732**	*0.787*	1.77×10^{-2}
28	$(-0.045, -0.026)$	**0.732**	*0.787*	3.10×10^{-2}
29	$(-0.020, 0.052)$	*0.785*	**0.810**	4.79×10^{-2}
30	$(0.020, 0.052)$	*0.785*	**0.810**	0.155
31	$(-0.015, -0.060)$	**0.880**	*0.824*	0.287
32	$(0.015, -0.060)$	**0.880**	*0.824*	1.08
33	$(0.045, 0.043)$	**0.880**	*0.824*	1.38
34	$(-0.045, 0.043)$	**0.880**	*0.824*	3.07
35	$(-0.060, 0.017)$	**0.880**	*0.824*	12.9
36	$(0.060, 0.017)$	**0.880**	*0.824*	15.7
37	$(0.025, -0.060)$	*0.924*	**0.890**	21.8
38	$(-0.025, -0.060)$	*0.924*	**0.890**	27.6
39	$(-0.040, 0.052)$	*0.924*	**0.890**	33.7
40	$(0.040, 0.052)$	*0.924*	**0.890**	41.7

(b)

No.	$\vec{k}/\lvert K_A\rvert$	$E_D(\vec{k})$	$E^{(0)}(\vec{k})$	$E^{(1)}$
1	$(0., -0.017)$	*0.244*	0.238	5.20×10^{-7}
2	$(0., 0.017)$	*0.244*	0.250	1.22×10^{-6}
3	$(-0.020, 0.017)$	**0.373**	**0.361**	2.13×10^{-5}
4	$(0.020, 0.017)$	**0.373**	**0.361**	0.928×10^{-4}
5	$(-0.020, -0.017)$	**0.373**	*0.384*	1.62×10^{-4}
6	$(0.020, -0.017)$	**0.373**	*0.384*	1.77×10^{-4}
7	$(-0.040, 0.017)$	*0.614*	**0.581**	2.03×10^{-4}
8	$(0.040, 0.017)$	*0.614*	**0.581**	2.85×10^{-4}
9	$(-0.040, -0.0174)$	*0.614*	*0.650*	3.12×10^{-4}
10	$(0.040, -0.017)$	*0.614*	*0.650*	5.04×10^{-4}
11	$(0., -0.052)$	**0.732**	0.682	6.35×10^{-4}
12	$(-0.020, -0.052)$	*0.785*	**0.756**	7.41×10^{-4}
13	$(0.020, -0.052)$	*0.785*	**0.756**	1.01×10^{-3}
14	$(0., 0.052)$	**0.732**	0.787	1.02×10^{-3}
15	$(-0.020, 0.052)$	*0.785*	*0.810*	1.11×10^{-3}
16	$(0.0201, 0.052)$	*0.785*	*0.810*	1.56×10^{-3}
17	$(-0.060, 0.017)$	**0.880**	**0.824**	1.56×10^{-3}
18	$(0.060, 0.017)$	**0.880**	**0.824**	2.05×10^{-3}
19	$(-0.04, 0.052)$	*0.924*	*0.890*	5.17×10^{-3}
20	$(0.040, 0.052)$	*0.924*	*0.890*	1.21×10^{-2}
21	$(-0.060, -0.017)$	**0.880**	**0.937**	9.92×10^{-2}
22	$(0.060, -0.017)$	**0.880**	**0.937**	0.111
23	$(-0.04, -0.052)$	*0.924*	*0.954*	0.116
24	$(0.040, -0.052)$	*0.924*	*0.954*	0.308
25	$(-0.06, 0.052)$	**1.11**	**1.01**	0.836
26	$(0.060, 0.052)$	**1.11**	**1.01**	1.25
27	$(-0.080, 0.017)$	*1.15*	*1.07*	2.14
28	$(0.080, 0.017)$	*1.15*	*1.07*	2.81
29	$(0., -0.087)$	1.22	1.08	3.53
30	$(-0.020, -0.087)$	**1.25**	**1.13**	4.48
31	$(0.020, -0.087)$	**1.25**	**1.13**	5.27
32	$(-0.080, 0.0522)$	*1.34*	*1.18*	6.24
33	$(0.080, 0.052)$	*1.34*	*1.18*	7.40
34	$(-0.060, -0.052)$	**1.11**	**1.22**	9.19
35	$(0.060, -0.052)$	**1.11**	**1.22**	11.8
36	$(-0.0804, -0.017)$	*1.15*	**1.22**	12.7
37	$(0.080, -0.0174)$	*1.15*	**1.22**	13.1
38	$(-0.040, -0.087)$	**1.34**	*1.28*	17.4943
39	$(0.040, -0.087)$	**1.34**	*1.28*	17.6
40	$(-0.100, 0.017)$	1.43	1.32	19.0

According to fig. 5, the main specific feature of the structure of electron levels of a toroidal GQD is self-similar energy bands located subsequently one after another on the energy scale. The atom-like distribution of the local electron density of states (LDOS) for some bands marked by dashed lines in fig. 5 is realized only for toroidal GQDs, from the geometric viewpoint, due to the absence of the curvature of a torus. These levels are occupied by electrons with wave functions of the type of standing waves (figs. 4 (upper row)). The electron density can be held also by the pseudopotential against the background of the constructive interference with the formation of strongly localized states (figs. 4(middle row)).

For the toroidal GQD, the electron density is absent on the quasi-zero-energy band due to the destructive interference of the states (figs. 4(lower row)). The last leads to the formation of a pseudogap between the hole and electron bands, providing the absence of the electron density at the center of the quantum dot, like the case of an ordinary atom.

C. Spherical quantum dot

Wave functions of S^2-QD in fig. 6a–d can be of two types: 1) localized state confined by the pseudopotential (see fig. 6a), 2) wave packages, whose electron density smears under the action of centrifugal forces stipulated by the

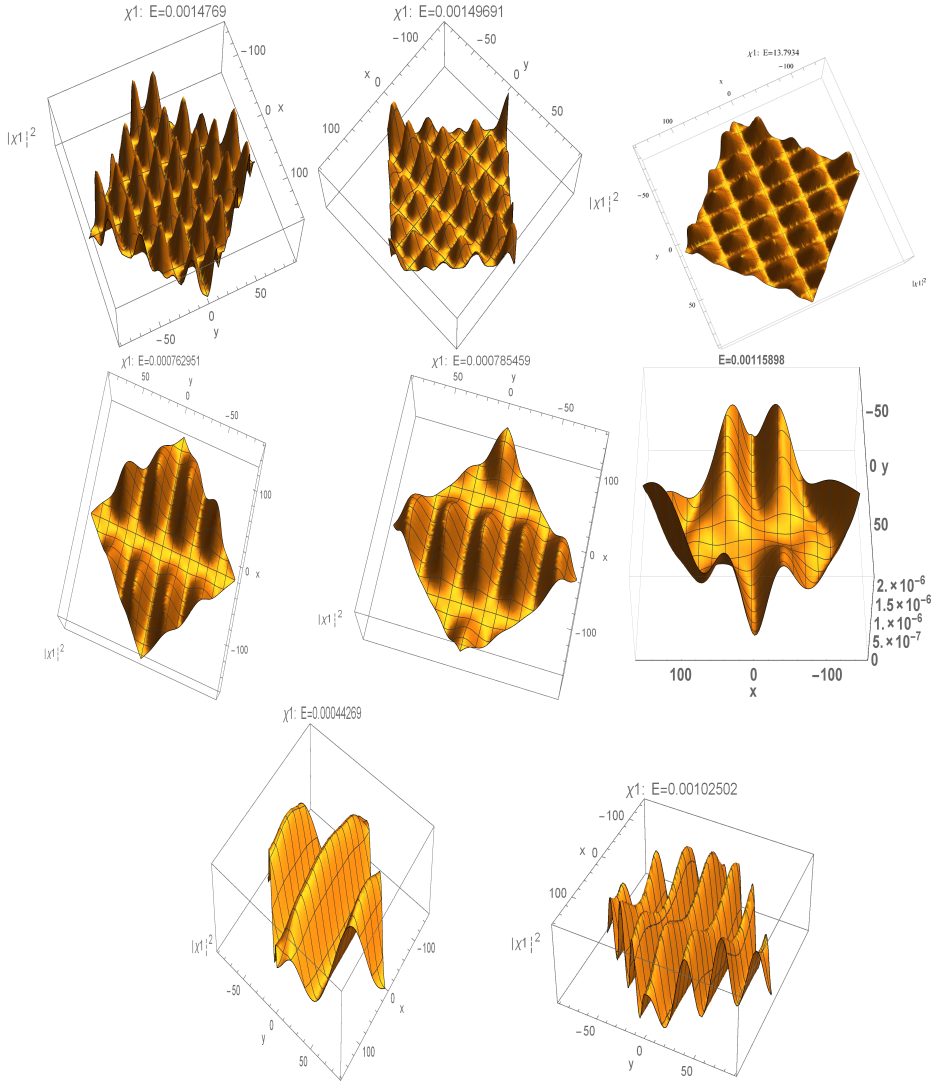

FIG. 4: Amplitude squares $|\chi|^2$ of states of the type of standing waves (upper row), strongly localized wave functions due to the pseudopotential confinement (middle row), weakly localized wave functions (lower row) for different energy levels of an $S^1 \times S^1$ dot; energy values E are in the insets.

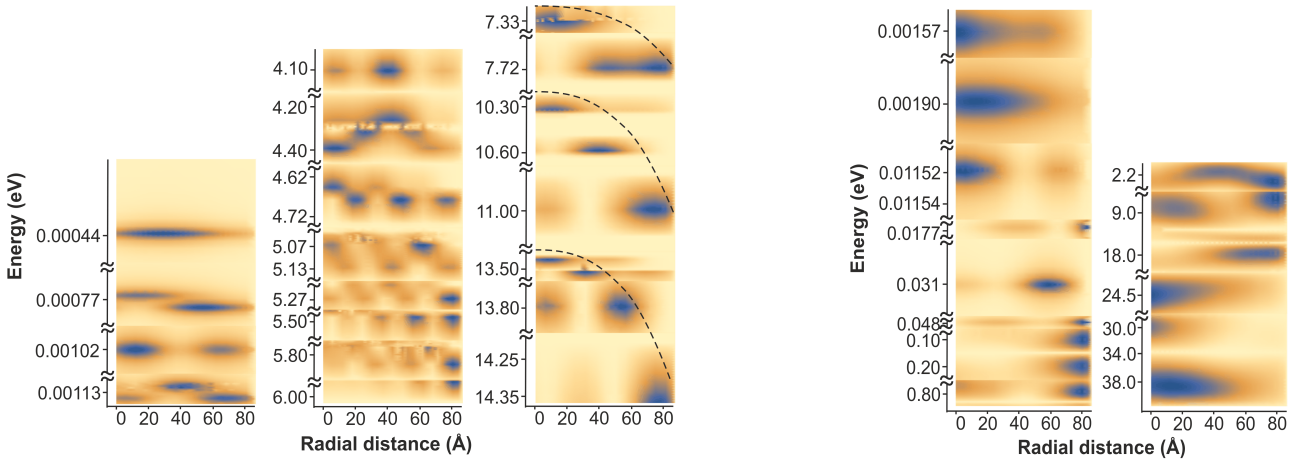

FIG. 5: LDOS of a toroidal quantum dot in bending bands. (to the left) LDOS for the states possessing high energes in the folding-zone approximation, (to the right) LDOS for the states possessing low energies in the folding-zone approximation. The self-similar bands are marked by dashed lines.

TABLE II: A set of eigenenergies $E^{(1)}$ for the continuous model GQD with the pseudopotential and its folding-zone approximation $E^{(0)}(\vec{k})$ with the torus (a) and sphere (b) topologies on sufficiently large energy scales. The degenerate levels are shown by a bold font and italics.

(a)

No.	$\vec{k}_i/\lvert K_A\rvert$	$E^{(0)}(\vec{k})$, eV	$E^{(1)}$, eV
1	(0.,-0.0522603)	0.682502	0.00044269
2	(0.,0.0522603)	0.787028	0.000762951
3	(-0.020115,-0.0871006)	**1.13688**	0.000785459
4	(0.020115,-0.0871006)	**1.13688**	0.00102502
5	(-0.020115,0.0871006)	*1.37428*	0.00112078
6	(0.020115,0.0871006)	*1.37428*	0.0011403
7	(0.,-0.121941)	1.44642	0.00132088
8	(-0.04023,-0.121941)	**1.61086**	0.00133497
9	(0.04023,-0.121941)	**1.61086**	0.0014769
10	(-0.020115,-0.156781)	*1.80494*	0.00149691
11	(0.020115,-0.156781)	*1.80494*	4.10456
12	(-0.04023,0.121941)	**1.97205**	4.28805
13	(0.04023,0.121941)	**1.97205**	4.32904
14	(0.,0.121941)	2.02188	4.39791
15	(0.,-0.191621)	2.05866	4.65659
16	(-0.060345,-0.156781)	**2.07966**	4.68424
17	(0.060345,-0.156781)	**2.07966**	5.03783
18	(-0.04023,-0.191621)	*2.1759*	5.04287
19	(0.04023,-0.191621)	*2.1759*	5.05353
20	(-0.020115,-0.226461)	**2.33715**	5.06723
21	(0.020115,-0.226461)	**2.33715**	5.1313
22	(0.,-0.261302)	2.53256	5.2241
23	(-0.0804601,-0.191621)	*2.53366*	5.26567
24	(0.0804601,-0.191621)	*2.53366*	5.46725
25	(-0.060345,-0.226461)	**2.54203**	5.49306
26	(0.060345,-0.226461)	**2.54203**	5.754
27	(-0.060345,0.156781)	*2.55864*	5.76914
28	(0.060345,0.156781)	*2.55864*	5.76979
29	(-0.04023,-0.261302)	**2.6196**	5.77387
30	(0.04023,-0.261302)	**2.6196**	5.83423
31	(-0.020115,0.156781)	*2.70447*	5.90736
32	(0.020115,0.156781)	*2.70447*	7.32916
33	(-0.020115,-0.296142)	**2.73993**	7.7165
34	(0.020115,-0.296142)	**2.73993**	10.3155
35	(0.,-0.330982)	2.88119	10.5945
36	(-0.060345,-0.296142)	*2.8931*	11.0023
37	(0.060345,-0.296142)	*2.8931*	13.4057
38	(-0.0804601,-0.261302)	**2.89342**	13.5148
39	(0.0804601,-0.261302)	**2.89342**	13.7934
40	(-0.04023,-0.330982)	2.94368	14.3684

(b)

No.	$\vec{k}_i/\lvert K_A\rvert$	$E^{(0)}(\vec{k}_i)$, eV	$E_i^{(1)}$, eV
1	(0.12069,-0.679384)	*2.98402*	0.141999
2	(0.648709,0.235172)	*2.98402*	0.173851
3	(0.140805,-0.644544)	**3.04794**	0.445753
4	(0.628594,0.200331)	**3.04794**	0.512985
5	(0.100575,-0.714225)	*3.08606*	0.527528
6	(0.668824,0.270012)	*3.08606*	1.14856
7	(0.628594,0.235172)	*3.08666*	1.61067
8	(-0.628594,0.235172)	*3.08666*	1.66149
9	(-0.12069,-0.644544)	**3.09133**	1.69783
10	(0.12069,-0.644544)	**3.09133**	1.97492
11	(-0.100575,-0.679384)	*3.11888*	2.22004
12	(0.100575,-0.679384)	*3.11888*	2.23016
13	(0.608479,0.200331)	**3.13245**	2.95946
14	(-0.608479,0.200331)	**3.13245**	3.09053
15	(-0.100575,-0.644544)	*3.17135*	3.55408
16	(0.100575,-0.644544)	*3.17135*	3.72894
17	(0.608479,0.235172)	*3.17135*	6.15254
18	(-0.608479,0.235172)	*3.17135*	6.22628
19	(0.648709,0.270012)	**3.18739**	6.27257
20	(-0.648709,0.270012)	**3.18739**	6.30184
21	(-0.12069,-0.609704)	*3.2017*	6.36295
22	(0.12069,-0.609704)	*3.2017*	6.37247
23	(0.588364,0.200331)	*3.2017*	6.42073
24	(-0.588364,0.200331)	*3.2017*	6.49724
25	(0.528019,0.409373)	**3.20443**	9.64421
26	(-0.528019,0.409373)	**3.20443**	10.0535
27	(-0.140805,-0.609704)	*3.20853*	10.8879
28	(0.140805,-0.609704)	*3.20853*	11.0748
29	(-0.100575,-0.609704)	**3.23346**	12.0065
30	(0.100575,-0.609704)	**3.23346**	12.3398
31	(0.588364,0.235172)	*3.23896*	12.7997
32	(-0.588364,0.235172)	*3.23896*	13.2614
33	(0.568249,0.200331)	**3.25623**	13.3698
34	(-0.568249,0.200331)	**3.25623**	13.5856
35	(0.16092,-0.609704)	*3.26342*	14.5628
36	(0.608479,0.165491)	*3.26342*	16.8546
37	(-0.0804601,-0.679384)	**3.26837**	16.8657
38	(0.0804601,-0.679384)	**3.26837**	16.8767
39	(0.548134,0.409373)	**3.26837**	18.0848
40	(-0.548134,0.409373)	**3.26837**	18.1502

curvature of a sphere (see fig. 6b–d).

According to fig. 7a,b, the main specific feature of the structure of electron levels of a spherical GQD, like that of a toroidal one, consists in the presence of self-similar energy bands placed subsequently one after another on the energy scale. States entering the wave package occur in the form of multi-resonance structure of LDOS in fig. 7. Electron density with such a structure is confined by staircase-like pseudopotential as one can see in fig. 7b,c. Opposite to the case of toroidal GQD, electron density is confined also on the quasi zero-energy band of spherical GQD (see fig. 7a). The confinement of the electron density of states of a type shown in figs. 4(middle row) and 6a has a form of non-structured regions of localization of LDOS and is observed for both spherical and toroidal GQDs.

D. Comparison with experimental data

We now compare the measured experimentally and theoretically predicted distributions of the electron density in an electrically confined monolayer GQD.

In [3], the atom-like structure of such type of GQDs has been studied. The GQD has been epitaxially grown up to a size of 8 nm along radius R on a copper substrate. It was shown that the states are strongly localized in space and are broadened in energy E. Such strong localization of broadened levels is not described by the Dirac equation with a confined cylindrical potential $V(R) = V_0\Theta(r_{dot} - R)$, since its solutions very narrow in E are spatially spread

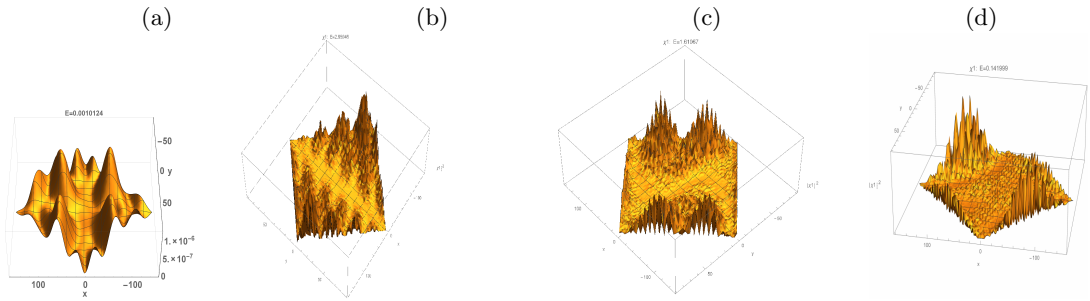

FIG. 6: Amplitude square $|\Psi|^2$ of spherical GQD: a localized state (a), wave packages (b–d); energy values E are in insets to figures.

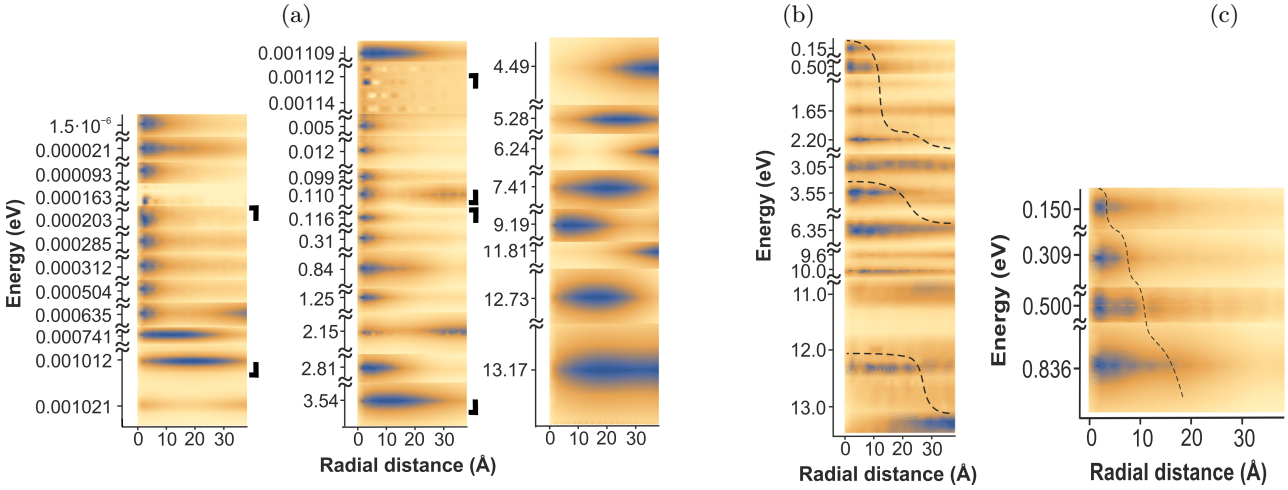

FIG. 7: LDOS of a spherical quantum dot in bending bands. (a) LDOS for the states possessing low energies in the folding-zone approximation; (b) LDOS for the states possessing high energies in the folding-zone approximation; (c) a band in the overlapping energy range. Self-similar bands are marked by dashed lines and bold angles.

over the whole GQD. In the continuous model, QGD with one Dirac point and 6 pairs of Weyl nodes–antinodes under the action of a pseudopotential, the states, like in the experiment, are strongly spatially localized similarly to atomic electron shells and are broadened in E (see fig. 8). Our numerical results, like the experiment ones, indicate that the parabolic potential is more adequate among confined potentials.

In [4], GQDs with a radius 150 nm were fabricated by the local embedding of a gate in a graphene/hexagonal boron nitride (BN) heterostructure on SiO_2, in order to exclude the influence of defects of a support. Let us compare fig. 9a and fig. 9b. Our numerical calculation of LDOS gives the levels with a multiresonance structure. These levels are completely analogous to multiresonance structures of the corresponding experimental GQD-bands.

In fig. 9c, we present the results of the description of this large GQD with the help of the Dirac equation with a parabolic potential. Consider GQD-levels formed at a positive bias V. The Dirac model of a radial GQD does not predict the highest experimental energy level of about 80-85 mV (this level is absent). Moreover, by predictions of the Dirac model, the levels with the same numbers of sites with spatial localization of the electron density (resonances) are arranged in pairs from 50 meV and lower. However, the doubling of the highest level of this band is not confirmed experimentally (see figs. 9b,c). The following drawback of the Dirac model is as follows: at a bias from 0 and lower, the number of levels in the experimental is twice less than that predicted theoretically.

Finally, consider the low-energy region from -50 to -100 mV (corresponding theoretically calculated levels are placed at -50 meV and lower). Contrary to LDOS in the Dirac model, the experimental LDOS and LDOS confined by the pseudopotential are redistributed to the GQD edge. Respectively, their hole density is polarized.

Let us compare the experimental data on electrically confined GQDs in a graphene monolayer covering a 30-nm-thick hexagonal boron nitride (BN) flake on graphite with the results of numerical calculations of our model GQD with sphere topology. The sphere has a nonzero curvature leading to a staircase-like pseudopotential in fig. 7c. This result is in complete agreement with the experimental fitting shown in fig. 2. The pushing out of electrons by the "centrifugal force" onto the quasi-zero-energy band is revealed as the nonzero electron density on its levels and is confirmed by the existence of the charging peaks of differential conductivity experimentally observed in [5].

By compensating the action of a pseudopotential, for example, by the Lorentz force, one can achieve a weak bending of the bands by a pseudopotential with the grouping of nondegenerate levels in the vicinity of the level degenerated

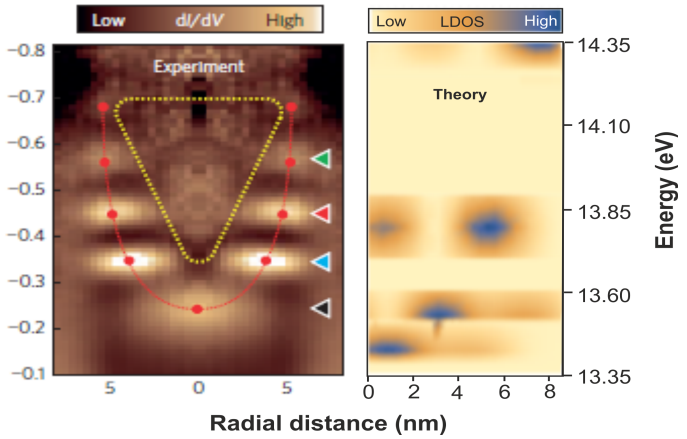

FIG. 8: Spectrum of atom-like spatially localized states of a GQD. (left) Spectroscopic map of GQD deposited on a copper substrate [3] as the dependence of the radially averaged derivative dI/dV of a STM-current I with respect to the bias V. (right) LDOS of the continuous toroidal model GQD under the action of a pseudopotential in the band of electron states of the type of standing waves located in the interval $13.35 \div 14.35$ eV.

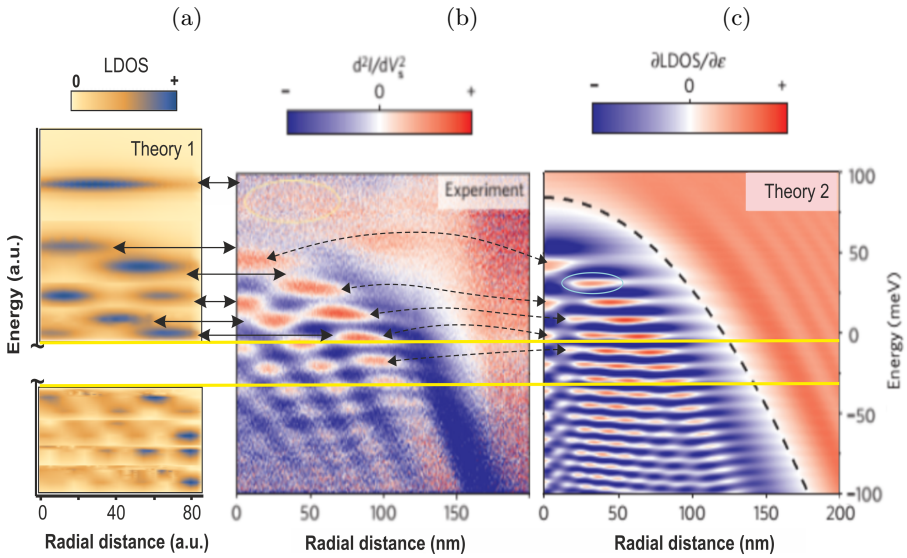

FIG. 9: Energy levels of spatially distributed states of a GQD. (a) Theoretically simulated LDOS in the bands of states confined by a pseudopotential on a background of a constructive interference for the continuous model GQD with torus topology (Theory 1). (b) Second derivative $\frac{d^2I}{dV^2}$ of a STM-current measured as a function of the bias V and the radial distance from the center of a circular graphene p–n junction deposited on BN/SiO_2, and (c) theoretically simulated first derivative of LDOS as a function of the energy and the radial distance for a parabolic potential [4] (Theory 2). Lines with arrows indicate to theoretical bands, coinciding with experimental ones. Experimental band, marked by yellow oval is predicted by Theory 1 and is absent in Theory 2. A theoretical band, marked by blue oval in fig. c, is experimentally unobservable.

in the folding-zone approximation. This mechanism explains the emergence of the level grouping in multiplets for an electrostatically confined monolayer GQD [5]. According to our theory, the values of the multiplicity are $p_d = 2, 4$, like in the experiment [5]. Moreover, the multiresonance distribution of LDOS over the energy levels of GQD with the sphere topology in fig. 7 leads the experimentally observed independence of the sequence of charging peaks of the distance of the cantilever STM tip to the GQD-center. The above discussion allows us to classify this electrostatically confined GQD on the BN/graphite support as a spherical one.

Thus, the theoretical predictions of the continuous model QGD with one Dirac point and 6 pairs of Weyl nodes–antinodes under the action of a pseudopotential not only explain, but show the excelent quantitative agreement with various experiments.

IV. CONCLUSION

So, we have described the confinement of electrons/holes in the rhombic graphene supercell. The quasiparticles are confined through polarization effects. The electrons/holes are localized in a pseudopotential that is calculated in the continuous approximation. The polarization of GQD due to the pseudopotential "pushes out" the energy levels, by removing their degeneration.

For a toroidal GQD, the quasiparticle states are partitioned into three types of bands. In the high-energy region due to the strong polarization of electron-hole pairs, the atom-like structure is formed in a parabolic potential well. The higher the polarization energy, the deeper the potential well. These electron/hole configurations are standing waves. For a toroidal GQD, the electron density on a quasi-zero-energy band is absent due to the zero curvature of a torus. This leads to the formation of a pseudogap between the hole and electron bands, which ensures the absence of the zero level at the center of QD, like at the center of an ordinary atom. In the intermediate energy region, the localization is observed only due to the pseudopotential.

The quasiparticle states of a spherical GQD form only two types of bands: a quasi-zero-energy band and the levels of confined wave packages.

To summarize, the quasirelativistic continuous models of graphene n-p-n (p–n–p) junctions with sphere and torus topologies have been proposed. A supercell pseudopotential which electrically confines electrons (holes) in a graphene quantum dot has been found. This potential bends energy levels in the parabolic way. For GQDs with the sphere topology, the parabolic potential is additionally modulated by staircase wise. This approach explains the main features of a local distribution of the electron GQD-density observed in various STM-experiments.

[1] Jia Zhang, Shu-Hong Yu, Materials Today. **19**, 382 (2016)
[2] N.N. Bogolubov, A.V. Soldatov, S.P. Kruchinin, Quantum Matter. **4**, 352 (2015)
[3] Ch. Gutiérrez, L. Brown, Cheol-Joo Kim, Jiwoong Park, A.N. Pasupathy, Nature Physics. **12**, 1069 (2016)
[4] Juwon Lee, Dillon Wong, Jairo Velasco Jr, J.F. Rodriguez-Nieva, Salman Kahn, Hsin-Zon Tsai, Takashi Taniguchi, Kenji Watanabe, Alex Zettl, Feng Wang, L.S. Levitov, M.F. Crommie, Nature Physics. **12**, 1032 (2016)
[5] N.M. Freitag, L.A. Chizhova, P.Nemes-Incze, C.R. Woods, R.V. Gorbachev, Y. Cao, A.K. Geim, K.S. Novoselov, J. Burgdörfer, F. Libisch, M. Morgenstern, Nano Lett. **16**, 5798 (2016)
[6] G. Giavaras, F. Nori, Phys. Rev. B **85**, 165446 (2012)
[7] P. A. Maksym, M. Roy, M. F. Craciun, S. Russo, M. Yamamoto, S. Tarucha, H. Aoki, J. Phys. Conf. Ser. **245**, 012030 (2010)
[8] K. Nakada, M. Fujita, G. Dresselhaus, and M. S. Dresselhaus. Phys.Rev. **B54**, 17954 (1996); H. P. Heiskanen, M. Manninen, and J. Akola,New J. Phys.10,103015 (2008). A.V. Rozhkov, G. Giavaras, Y.P. Bliokh, V. Freilikher, F. Nori. Physics Reports. **503**, 77 (2011).
[9] M. Grujic, M.Zarenia, A. Chaves, M.Tadic, G.A. Farias, F.M. Peeters. Electronic and optical properties of a circular graphene quantum dot in a magnetic field: Influence of the boundary conditions. Phys. Rev. bf B 84, 205441 (2011)
[10] A. Müller, B. Kaestner, F. Hohls, T. Weimann, K. Pierz, H.W.J. Schumacher. Appl. Phys. **115**, 233710 (2014)
[11] L.L. Li, M. Zarenia, W. Xu, H.M. Dong, F.M. Peeters. Exciton states in a circular graphene quantum dot: Magnetic field induced intravalley to intervalley transition. Phys. Rev. B **95**, 045409 (2017)]
[12] J.-R. Wang and G.-Z. Liu, J. Phys.: **Condens. Matter 23**, 155602 (2011).
[13] S. Reich, C. Thomsen, J. Maultzsch. Carbon nanotubes. *Basic Concepts and Physical Properties.* (WILEY-VCH Verlag GmbH & Co. KGaA, Wenheim, 2004)
[14] H.V. Grushevskaya, G. Krylov, J. Mod. Phys. **5** 984 (2014).
[15] H. V. Grushevskaya and G. Krylov, Int. J. Nonlin. Phen. in Compl. Sys. **18**, 266 (2015)
[16] V.A. Fock, *Fundamentals of Quantum Mechanics* (Mir Publishing, 1978)
[17] H. Krylova, L. Hurski, *Spin polarization in strongly correlated systems.* (LAP Lambert Academic Publishing, 2013)
[18] V. V. Kudryashov, Int. J. Nonlin. Phen. in Compl. Sys. **12**, 199 (2009)